
Ca' Foscari University of Venice



Ca' Foscari University of Venice

Department of Molecular Sciences and Nanosystems

Master's Degree Programme in Science and Technology of Bio and Nanomaterials

# Towards 3D Luminescence Thermometry

## An approach based on lanthanide nanoparticles and dimensionality reduction techniques

**Supervisor**

Prof. Patrizia Canton

**Assistant supervisor**

Dr. Erving Ximendes

**Graduand**

Anna Romelli

890700

**Academic Year**

2022 / 2023

# Index of contents

# 1. Abstract

Luminescence nanothermometry is a contactless technique efficiently used for temperature measurements in biological applications. It takes advantage of the thermal dependence of nanoparticles optical properties, such as luminescence lifetime and spectral features (e.g. intensity, shift, peak width). Different types of probes are available for this purpose, among which there are lanthanide-doped nanoparticles. Compared to thermometers based on lifetime, spectral-based nanothermometers are highly affected by the presence of a biological tissue, because photon-tissue interactions introduce distortions in the shape of the emission spectrum, resulting in erroneous thermal readouts.

The aim of this project was to explore the possibility to take advantage of these tissue-induced spectral changes to build-up the case for 3D image reconstruction, rather than for thermal applications. Emission spectra of nanoparticles doped with lanthanide ions ($NaYF_4$@$NaYF_4$:Nd,Yb@$CaF_2$) were collected, knowing that their features were dependent on the thickness of the tissue. To mimic the biological environment, tissue phantoms were prepared, and they were placed on top of NPs to collect hyperspectral images of the sample. By means of dimensionality reduction techniques (specifically Principal Component Analysis), the dependence of emission spectral changes with the thickness of the tissue was investigated. This analysis led to a new representation of the system that was finally used to develop a regression model for the 3D image reconstruction of a simple conic-shaped tissue.

# 2. Introduction

## 2.1. Photoluminescence

According to IUPAC, luminescence is defined as the "spontaneous emission of radiation from an electronically or vibrationally excited species not in thermal equilibrium with its environment" [1]. It can be classified in different ways depending on the type of excitation source; of particular interest is photoluminescence, the phenomenon of direct excitation of an atom or molecule due to the absorption of photons. The energy absorbed from the electromagnetic radiation, allows the electrons of the material to jump towards a more energetic level, which is, however, less stable. Due to this instability, a relaxation process occurs and electrons return to the ground state, releasing part of the energy absorbed in the form of light.
Photoluminescence can be divided into fluorescence and phosphorescence (Fig. 1). Fluorescence is the result of the relaxing electronic transition between an excited level and the ground level, both in singlet state; in this case, the average lifetime of a typical emitting excited state is in the order of nanoseconds. On the contrary, phosphorescence is the radiative decay from a triplet state, once that excited electrons undergo an intersystem crossing process; for those excited states, the average lifetime goes from microseconds to hours [2, 3].

The first application of photoluminescence as experimental technique dates back to the 1950s, when it was used to explore the optical properties of Germanium. However, it became a widespread technique only in the following decade, with the availability of different laser sources [4], which are optically stable and very intense. Photoluminescence can be used to investigate electronic transitions by looking at the position of bands, as well as to identify type and concentration of impurities in a material by looking at linewidths and peak energies. Moreover, measures of photoluminescence as a function of temperature, enable the analysis of nonradiative centers and their thermal activation energy [4].
Nowadays, luminescence finds application in many different fields: in optoelectronic devices, such as displays, LEDs and fluorescent lamps; in organic substances used in forensic applications [2]; in biotechnology, for assays based on fluorescent proteins, such as GFP [5]; in biomedicine, in the luminescent probes used for imaging [6], etc.

## 2.2. Lanthanide ions

Concerning potential biological applications of luminescent materials, of particular interest are the nanoparticles doped with lanthanide ions. Contrary to other kinds of luminescence materials, such as semiconductor nanocrystals, in which the optical properties are generated at the whole particle level, in lanthanide-doped NPs the luminescence arises from the localized luminescent ions. This feature enables tuning the optical properties by means of controlling the nature and amount of introduced ions.

Lanthanides are the chemical elements of the f-block of the periodic table, included between Cerium (Ce, Z=58) and Lutetium (Lu, Z=71) (Fig. 2a). Together with Yttrium and Scandium, these elements are also known as “rare earth elements”, and one of their most intriguing features is their similarity in chemical properties. A simple explanation can be found by looking at their electronic configuration, especially if considering their derived ions which essentially exist in a trivalent state ($Ln^{3+}$) and whose electronic configuration is (Fig. 2b):

$$Ln^{3+} = [Xe]4f^{(0\text{-}14)}$$

The fascinating fact of this configuration is that, even though the 4f level is more energetic, it is shielded by the filled $5s^2 5p^6$ sub-shells, so that 4f orbitals are not involved in the formation of bonds with other elements. The optical properties of $Ln^{3+}$ ions stem from transitions involving 4f electrons, and the "buried" nature of these orbitals is at the origin of the uniqueness of the spectroscopic properties of $Ln^{3+}$. [7, 8, 9].

There are three types of electronic transitions involving lanthanide ions: 4f–4f transitions, 4f–5d transitions, and charge-transfer transitions, each promoted by a different operator related to the nature of light (the odd-parity electric dipole operator, the even-parity magnetic dipole operator, and the electric quadrupole operator) [7, 10]. Since they have to obey specific selection rules, not all the transitions are permitted. One of these rules is valid for molecules that are centrosymmetric and is known as Laporte’s parity selection rule. It states that electronic transitions between states with the same parity are forbidden: this implies that, in principle, f–f transitions in $Ln^{3+}$ ions should be not allowed.

Nevertheless, this rule is relaxed when the lanthanide ion is inserted into a crystal field, because non-centrosymmetric interactions allow the mixing of electronic states of

opposite parity into the 4f wavefunctions, so that the Hamiltonian describing electrons in 4f orbitals is perturbed [7]. At this point, these transitions become partially allowed, in the sense that they have a certain (not zero) probability to happen, and hence they can be detected (Fig. 3a).

Actually, different types of processes can occur between ions to enable these transitions (Fig. 3b). One example is the so-called upconversion, a phenomenon in which low energy electromagnetic radiation, typically in the near infrared (NIR) range, is converted into higher energy light in the visible (Vis) or ultraviolet (UV) range; in this case, the frequency of the emitted photons is higher than the frequency of the excitation photons ($h\nu_{em} > h\nu_{ex}$). Upconversion is unique because the absorption of multiple photons occurs in a sequential fashion (no need of simultaneous absorption, like in the case of e.g., two-photon luminescence). This is possible because of the long-lived nature of the $Ln^{3+}$ 4f levels, originating from their forbidden nature.
The opposite happens instead for a downshifting process: the energy of the light emitted is lower than the energy of the light used for the excitation ($h\nu_{em} < h\nu_{ex}$), meaning that some part of the energy is distributed elsewhere, generally lost in the form of heat through lattice vibrations. [11, 12].

The f–f emission lines of lanthanide ions cover the entire spectrum, from UV ($Gd^{3+}$) to visible (e.g., $Pr^{3+}$, $Sm^{3+}$, $Eu^{3+}$, $Tb^{3+}$, $Dy^{3+}$, $Tm^{3+}$) and near-infrared (e.g., $Pr^{3+}$, $Nd^{3+}$, $Ho^{3+}$, $Er^{3+}$, $Yb^{3+}$) wavelengths [7, 10, 13, 14]. These transitions are easily recognizable both in the absorption and in the emission spectrum, because they are characterized by specific and easily distinguishable features. First of all, their bands in the spectra are narrower compared to other transitions (Fig. 4a), since the rearrangement that follows the excitation of the electron into a 4f orbital does not really affect the binding pattern of the molecules. Another consequence of this behaviour is the very small Stoke's shift - i.e., the energy separation between absorption and emission through the same electronic transition - due to the fact that, in the excited state, internuclear distances remain almost the same (Fig. 4b) [7]. In addition, the fact that 4f-4f transitions are forbidden results in longer lifetimes $\tau$ of the excited states, which measure from micro to milliseconds (Fig. 4c) [9].

Two other very important parameters that must be considered describing $Ln^{3+}$ photoluminescence are the quantum yield $Q$ and the brightness $B$. The photoluminescence quantum yield can be defined in a general way as:

$$Q = \frac{number\ of\ emitted\ photons}{number\ of\ absorbed\ photons}$$

Considering the direct excitation of the 4f levels, it is possible to define a more specific quantity, the intrinsic quantum yield $Q^{Ln}$ , as:

$$Q^{Ln} = \frac{k_{rad}}{k_{obs}} = \frac{\tau_{obs}}{\tau_{rad}}$$

where $k_{obs}$ is the rate of depopulation of the excited level, and $k_{rad}$ is the radiative rate constant [7, 15]; they are, in turn, related to the reciprocal of the states' lifetimes. Both radiative and non radiative processes are included in the rate constant $k_{obs}$, which can be described as:

$$k_{obs} = k_{rad} + \sum_n k_n^{not\ rad}$$

In absence of nonradiative deactivation processes, $k_{obs}$=$k_{rad}$ and the quantum yield would be equal to 1, which is a very rare event [7].

However, especially regarding biological applications and sensing, a more comprehensive and meaningful parameter for luminescent nanoparticles is the brightness $B$. It is the product of luminescence quantum yield $Q$ and the molar absorption coefficient at the excitation wavelength, $\varepsilon(\lambda)$ [15]:

$$B = Q \cdot \varepsilon(\lambda)$$

Since the quantum yield is dimensionless, $B$ has the unit of $M^{-1}cm^{-1}$.
To have more precise readouts, having a high value of quantum yield is not sufficient: what needs to be large is the value of the brightness, that is directly related to the amount of signal.

## 2.3. Biological applications of luminescent NPs

### 2.3.1. Luminescence thermometry

Focusing on the biological field, one important application of luminescent NPs is the realization of luminescent nanothermometers (LNThs). LNThs take advantage of the thermal dependence of optical and spectroscopic properties of the particles: when a change in temperature occurs, one of the parameters describing the emitted light are modified. These parameters can be, for instance, the intensity of the luminescent bands, the shape of the emission spectra or the luminescence lifetime. If the mechanism that induces such changes is known and can be modelled using some equations, this system is called a primary thermometer [2, 16]. Different kinds of luminescent probes are available for this purpose, especially for biomedical applications, including quantum dots, semiconductor nanocrystals, polymers, metal–organic frameworks and lanthanide- or transition metal-doped nanomaterials [17]. In particular, thermometers based on lanthanide ions are versatile and stable, have narrow emission bands with as high as emission quantum yields [14]. A big advantage of luminescence thermometry is the fact that it is contactless, enabling remote thermal readout of the environment where the probe is. As a consequence, this type of thermometry could be used as a tool for the early diagnosis of several diseases, as well as for improving the efficacy of thermal therapies, being a minimally invasive, cost-effective, and experimentally simple technique [16, 18].

Although luminescence nanothermometry is in its early stages, a good number of preclinical applications have already been demonstrated, and this is also due to the appearance of more and more luminescent nanothermometers working in the so-called biological windows (BWs) [2, 16]. The main feature of these spectral regions is that scattering and absorption coming from biological tissues are highly reduced, enabling a deep-tissue penetration of light. The ranges of the biological windows are defined considering the absorption bands in the spectrum of water (Fig. 5):

- 650–950 nm → first biological window (I-BW)
- 1000–1350 nm → second biological window (II-BW)
- 1400–1900 nm → third biological window (III-BW) [2, 17].

These intervals must be taken into account for a proper selection of excitation and emission wavelengths because, in addition to the issues related to the limited penetration depths, BWs can help in reducing the high background signals arising from emission of endogenous fluorophores of the tissue (e.g., NADH, FAD, DNA, proteins, or collagen) (Fig. 5) [17].

Luminescent thermometry can be classified based on the different sensing method, each one taking advantage of a specific temperature-dependent mechanism (Fig. 6). The main examples are:

1) spectral shift of a given transition;
2) emission intensity measurements, by using the integrated intensity of a single transition, the ratio between the intensity of two different transitions, or also the changes in the width of peaks;
3) lifetime measurements, based on the decay curves of the emitting excited states [14, 17].

Luminescent thermometers based on the emission intensity of a single transition depend critically on the fluctuations of the excitation source and the local changes of the phosphor concentration. Therefore, in general, thermometers that detect temperature changes by the luminescence intensity ratio of two emission bands are chosen. However, as will be discussed later, the shape of emission spectra is highly influenced by the presence of a biological tissue, and this could be a relevant problem for biomedical applications. Lifetime-based sensing methods do not suffer from such disadvantages, but they require longer acquisition times, post-processing techniques, and usually a more complex instrumentation [14].

For each thermometer, the thermometric parameter Δ(T) can be defined, which is the spectroscopic parameter that provides the thermal readout. Once that Δ(T) is established, different figures of merits can be used for the performance comparison of luminescence thermometers. Among them, the relative thermal sensitivity $S_R(T)$ indicates the relative change of Δ(T) per degree of temperature, and its percentage value is given by:

$$S_R(T) = \frac{1}{\Delta(T)}\left|\frac{\partial\Delta(T)}{\partial T}\right| \cdot 100 \quad [\% \cdot {}^{\circ}C^{-1}]$$

where $\left|\frac{\partial\Delta(T)}{\partial T}\right|$ is the so-called absolute thermal sensitivity [14, 17]. Another relevant figure of merit is the temperature uncertainty $\delta T$ (called also thermal resolution): it determines the minimum temperature difference detected by a thermometer under specific experimental conditions. It is defined as:

$$\delta T = \frac{\partial T}{\partial \Delta(T)} \cdot \delta\Delta(T)$$

where $\delta\Delta$ is the uncertainty in the determination of the thermometric parameter. The value obtained for $\delta T$ allows the comparison between thermometers without considering the nature of the thermometer itself and the thermometric parameter $\Delta$(T) [18].

Other figures of merit which can be used are the brightness, which allows to have reliable signals even maintaining a low photoexcitation intensity and a low concentration of nanoparticles, and the spatial and the temporal resolution of the thermometer [2, 17].

### 2.3.2. Light-tissue interaction and its effects in thermal readouts

A fundamental process that must be understood dealing with biological applications of luminescent NPs, is the interaction of the light with both the particles and the biological tissues. In an organism, optical properties of tissues can change passing from one tissue to another. Sometimes these are dramatic variations, as it is the case, for instance, at interfaces between soft biological tissue and bone tissue [19].
The main phenomena occurring when light interacts with a tissue include, in general, reflection (at the material interface), refraction (if the two tissues have different refractive indexes), absorption and scattering of photons in the material (Fig. 7).

The light absorbed can undergo different competing mechanisms: it can be converted into heat, radiated in a photoluminescence process or consumed in photo-chemical reactions. To quantitatively describe this phenomenon, the absorption coefficient $\mu_a$ of the material (which is in this case a biological tissue) can be defined: it determines how far light with a specific wavelength can penetrate into the tissue, and also how much energy the tissue absorbs from a particular optical source [19]. The scattering coefficient $\mu_s$ can be defined as well, in order to describe how photons of the incoming light are

scattered from their original path by the different components of the tissue. In general, for describing tissue's optical properties, the reduced scattering coefficient $\mu_s'$ is preferred, since it considers also the anisotropy factor *g* of the tissue (which is defined as the average cosine of the scattering angle); it can be computed as follows:

$$\mu_s' = (1 - g)\mu_s$$

Depending on the application and on the feature of the tissue, these coefficients assume different importance: for very thin tissue (<1 mm) it is preferable to have a correspondence in the absorption coefficient, the scattering coefficient, and the anisotropy coefficient; for larger thicknesses, a comparable reduced scattering coefficient is all that is required [22]. These optical properties, together with the refractive index, are specific for each material, and can be used to understand the way in which the detected signal can be attenuated.

This attenuation is what usually happens for spectral-based thermometers working in *in vivo* conditions; in fact, in those cases, not only the emission signal is attenuated by the tissue, but the shape of the emission spectra is also distorted. Indeed, the fact that the luminescent nanothermometer works in the biological windows where a maximized depth of penetration of light is assured, is not sufficient to guarantee the lack of spectral distortions. Actually, the collected luminescence has not the same spectral properties as the luminescence generated by the nanothermometers located in a deeper position inside the tissue, due to the wavelength dependence of the optical properties of the tissue itself; this gives rise to distortions in the shape of the spectra, that could induce artifacts and relevant errors in the determination of the temperature [16].

Nevertheless, thermal readouts obtained from emission spectra are not the only results influenced by the presence of a biological tissue, since the readouts based on lifetime are affected too. The reason for this can be attributed to the scattering phenomena induced within the tissue, which cause the deviation of photons trajectory from a purely ballistic to a non-ballistic one (Fig. 8).

Starting from these considerations, Shen et al. have calculated the error in the temperature determination of lifetime-based nanothermometers [20]. Due to scattering events, the average path length travelled by a photon within the tissue is larger than the thickness of the tissue itself. For this reason, it takes more time for scattered photons to cross the tissue, with respect to photons travelling along ballistic trajectories. This time delay causes an increase in the detected fluorescence lifetime, which, in turn, leads to a discrepancy between the real sub-tissue temperature and the temperature obtained translating the measured lifetime through the calibration curve. Nevertheless, even though the photon scattering constitutes a source of error, its magnitude is generally much lower than the one of the uncertainty obtained when temperature is evaluated from the spectral analysis (tenth of °C with respect to few degrees). For this reason, by working with lifetimes, the effect of the tissue-induced temperature uncertainty can be considered negligible in the conditions generally encountered in *in vivo* measurements (i.e., lifetimes >100 ns and tissue thickness < 1 cm) [20].

As regards this project, the first idea was to create a sort of self-calibrated nanothermometers, using lifetime calibrations to correct thermal readouts coming from NPs emission spectra in the presence of tissue phantoms. However, during the measurements some results enabled the project to change with respect to the original idea, exploring the possibility of building-up the case for 3D image reconstruction.

# 3. Materials and Instruments

***Tissue phantoms preparation - Materials***

- Agar (Sigma Aldrich, CAS: 9002-18-0)
- Intralipid® - 20% emulsion, phospholipid stabilized soybean oil (Sigma Aldrich, CAS: 68890-65-3)
- Absolute ethanol
- Distilled water

***Equipment***

- 50 mL beaker
- P100 and P500 micropipettes
- 15 mL graduated cylinder
- Heating plate with magnetic stirrer
- Plastic cuvettes

***Instruments***

*Heating plate*: it allows to change temperature up to tenth of °C during the measures.

- Lifetime measurements : T range 32.0-46.0°C - step: 2.0°C;
- Emission measurements : T range 30.0-45.0°C - step: 1.0°C.

*Thermocouple for surfaces*: was used to measure the real temperature of the Q-pod and of the heating plate, together with PicoLog TC-08 thermocouple data logger. In Appendix 1 are reported the data of real temperature recorded every time the heating plate was involved in a measure.

*Optical Parametric Oscillator (OPO)*: lifetime measurements were performed by using an Optical Parametric Oscillator (Lotis TII) pumped by a frequency tripled Nd:YAG laser; the OPO works at 800 nm wavelength and it provides 10 ns pulses. The emitted radiation was collected and spectrally filtered by a high-brightness monochromator (Shamrock 163, Andor), equipped with two gratings: 1) blaze = 1700 nm, 75 g $mm^{-1}$ for NIR emission and 2) blaze = 500 nm, 300 g $mm^{-1}$ for visible emission. Time evolution was recorded by an infrared photomultiplier (Hamamatsu H1033C) connected to a digital oscilloscope (Le Croy Wave Runner 500).

*UV/Vis/NIR Spectrophotometer*: extinction spectra of tissue phantoms and absorption spectra of water were measured with a double-beam spectrophotometer (Lambda1050, Perkin Elmer) working in absorption mode. It allows measuring in both UV/Vis and NIR range, being equipped with three detectors: PMT Si (for $\lambda$<900 nm), InGaAs (for $\lambda$=900-1500 nm), PbS (for $\lambda$>1600 nm).

*Q-pod*: Peltier temperature controller (Q-pod 3e, Quantum Northwest) was used to investigate the evolution with temperature of the phantom extinction spectrum and the water absorption spectrum.

*Hypercube:* to collect emission spectra, HyperSpectral imaging (HSI) was performed. Regarding the optical set up, the excitation is provided by an 808 nm fiber-coupled laser diode, in front of which, a 810 nm band-pass filter (ThorLabs, FB810) is placed in order to filter the excitation wavelength. For building the hyperspectral image, a set of lenses is used to image the pupil on a Bragg tunable filter (BTF). This filtered light is then focused, by a second lens, on an infrared camera (ZephIRTM 1.7) to produce a monochromatic image. Synchronous tuning of the BTF and image acquisition allows to obtain the monochromatic fluorescence images corresponding to different emission wavelengths. In this way, a 3D spatial map of spectral variation (HSI cube) can be built: the first two dimensions provide spatial information and a third dimension accounts for the spectral information. The intensity values of a particular pixel in a HSI cube characterized its spectral fingerprint [16].

*Pictures and details of experimental set-up are reported in Appendix 2.*

# 4. Project

## 4.1. Original idea

As already discussed, one of the main challenges of spectral-based nanothermometry is the collection of reliable signals and reliable thermal readouts through different tissues of an organism. Trying to provide a solution to this problem, the original idea of the project is to create a sort of "self-calibrated" nanothermometers based on luminescent nanoparticles doped with lanthanide ions. In particular, the aim is to exploit the temperature-dependence of NPs lifetimes to create a calibration with temperature; later, this lifetime-based calibration will be used for the correction of the calibration resulting from the emission measurements of the same NPs. The final goal is then to evaluate if the resulting method for this "auto-calibration" could be applied also to other types of spectral-based thermometers.

## 4.2. Lanthanide doped luminescent NPs

A water dispersion of lanthanide doped core/shell/shell nanoparticles was used for this project (c = 13 mg/ml)*:*

$$NaYF_4@NaYF_4{:}Yb^{3+},Nd^{3+}@CaF_2@PAA \text{ in water}$$

*(It was synthesized by the group of professor Jorge Rubio-Retama in the department of Química en Ciencias Farmacéuticas of the Complutense University of Madrid, which collaborates with the NanoBIG group. They also provided a first characterization of such NPs, shown in Fig. 9).*

The sodium yttrium fluoride ($NaYF_4$) core of the NPs had a diameter around 7 nm; $NaYF_4$ is efficiently used as host materials for lanthanide luminescence because it has low lattice phonon energy that minimizes multiphonon nonradiative processes of excited states [21]. The inner shell of the particles (size ~11 nm), was doped with $Yb^{3+}$ and $Nd^{3+}$ ions, in the optimal doping level known to be 20% and 60% respectively [21]. The outer shell instead was made of $CaF_2$ (size ~18 nm); this material allows to enhance biocompatibility and to shield the luminescent middle shell from surface quenching processes [21]. The surface of the NPs was then functionalized with molecules of Polyacrylic Acid (PAA) to allow their dispersibility in water (Fig. 9a).

As a first analysis, emission spectra were recorded at different temperatures, demonstrating the temperature dependence of the peaks' intensity (the spectra were not normalized). The intensity ratio of the signal centered at 980 nm and 1060 nm was used as the thermometric parameter to calculate the percentage relative sensitivity of a spectral-based thermometer made by these NPs, which results to be $S_R$ = 1.12% °$C^{-1}$ (Fig. 9b and c). In addition, from the decay curves of the NPs it was computed the luminescence lifetime: the value obtained was $\tau \simeq 210\mu s$ and it was already demonstrated to be temperature-dependent [21].

Based on these results, the use of such NPs seemed to be the best choice for the realization of the project, having both lifetime and emission dependent on temperature. In particular, the phenomena exploited by these NPs for temperature determination are the energy transfer (ET) and back energy transfer (BET) mechanisms between $Nd^{3+}$ and $Yb^{3+}$ ions (Fig. 10a). $Nd^{3+}$ ions are excited in the first biological window with a 808 nm light, since this optical excitation leads to a minimum thermal loading and so it's preferred for in vivo applications instead of another common wavelength: 980 nm. Then, thanks to a non-radiative process, the energy is transferred to $Yb^{3+}$ ions, which act as activators, emitting photons of wavelength around 980 nm in the second biological window. It must be considered that $Nd^{3+}$ ions can also undergo radiative processes, due to electronic transitions from an excited level to the ground level. However, contrary to the $Yb^{3+}$ emission signal at 980 nm, the $Nd^{3+}$ radiative transitions are not so easily visible in the emission spectra of the particles (Fig. 10b). It is possible to recognize the emission at 1060 nm even though it does not appear as a clear peak, being broader and overlapped to the Yb emission band: this overlapping is what indicates a very efficient energy transfer between lanthanide ions.

## 4.3. Tissue phantoms

### 4.3.1. Introduction

To simulate an environment that reproduces a biological one in which luminescent nanoparticles or nanothermometers can be potentially used, so-called tissue phantoms were fabricated. The production of phantoms is a useful and inexpensive technique that allows the study and the optimization of new systems before the transition to some clinical application. Their big advantage is that their absorption and scattering coefficients are known, and they can be modulated changing the concentration of the tissue phantoms components.

Different factors must be considered during the design of phantoms: geometrical parameters, such as thickness and shape, the wavelength range in which they will be applied, or the compatibility for the inclusion of biologically relevant chromophores and fluorophores. For optical and NIR spectroscopy, where the spectral sensitivity to molecular features of tissue is very important, the development of reliable tissue phantoms is required. To make this possible, non-organic and silicone phantoms are substituted by biologically compatible structures such as agar, gelatin, or collagen matrices that allow the easy inclusion of cellular constituents, such as blood, fat and/or other exogenous luminescent molecules [22]. Regarding the scattering agent, its choice is usually separated from the choice of the matrix, since the volume fraction of the scattering material is typically less than 5% of the total. The most widely used scattering agent is a commercially available lipid emulsion named Intralipid®, but other options, still based on lipid or polymer microparticles, are possible [22].

### 4.3.2. Tissue phantoms preparation

Before starting the measurements, tissue phantoms were prepared, by selecting as the scattering agent Intralipid® (20% emulsion). In order to make a calibration of the extinction coefficient of the tissue, 5 different phantoms with 5 different compositions were prepared (Tab. 1). The relative content of the Intralipid® emulsion for each batch was: 0%, 0.2%, 0.5%, 1%, 2% (of the total volume).

For the preparation, a 50 ml beaker with the proper amount of water was placed into a pre-heated oil bath at 110 °C. Different volumes of Intralipid® were pre-dissolved in a minimal amount of ethanol and then added to the water; the beaker was covered and the

mixture was kept under stirring (600 rpm) until boiling. Next, 2 wt.% of agar powder was added and left with heating and stirring until the agar was completely dissolved (~15 minutes). After this time, the temperature of the oil bath was decreased to 80°C and the cover was removed to let the ethanol evaporate (~2 minutes). Finally, the mixture was poured into the final container and allowed to cool to room temperature until the gel was set.

| | V tot. = 15 ml | | |
|---|---|---|---|
| Intralipid® relative content % | $V_{Intralipid®}$ (µl) | $V_{water}$ (ml) | $m_{agar}$ (mg) |
| 0 | 0 | 15 | 300 |
| 0.2 | 30 | 14.970 | 300 |
| 0.5 | 75 | 14.925 | 300 |
| 1 | 150 | 14.850 | 300 |
| 2 | 300 | 14.700 | 300 |

***Tab. 1** - Precursors' quantities used for the preparation of tissue phantoms with different composition.*

### 4.3.3. Optical characterization of phantoms: extinction measurements

To evaluate the optical properties of a tissue, the extinction coefficient has to be considered [23]:

$$\mu_{ext} = \mu_{scatt} + \mu_{abs}$$

where $\mu_{scatt}$ is the scattering coefficient and $\mu_{abs}$ is the absorption coefficient. To measure $\mu_{ext}$, optical extinction spectra of tissue phantoms were recorded at room temperature by means of a UV/Vis/NIR spectrophotometer, in the wavelength range between 400-1800 nm (step 4 nm). The samples for these measurements were prepared by cutting a slice of about 1 mm thickness for each tissue phantom with a different composition; this slice was then placed in between two microscope slides (Fig. 11).

For each sample the measure was collected in 3 different regions of the tissue, to have the best possible approximation of the optical properties of the whole tissue. Once the spectra were collected, the extinction coefficients $\mu_{ext}$ were calculated based on the Beer-Lambert law and knowing that the intensity of the signal decreases exponentially with the distance travelled by the light:

$$I \sim I_0 \cdot e^{-\mu d}$$

where $I_0$ is the intensity of the incoming light; I is the intensity of the transmitted light; μ is the extinction coefficient of the tissue, d is the optical path length. The results obtained are reported in (Fig. 12a).

From these spectra it is possible to evidence that, considering the visible range (λ<800 nm), the effect of the scattering increased as the relative content of Intralipid® increased. In addition, in all cases, there are three bands centred respectively at ~1000 nm, ~1200 nm and ~1500 nm, originating from the absorption of water. For comparison, in fig. 12b the absorption coefficient spectrum of water is shown, collected at room temperature in the same wavelength range (400-1800 nm), where it is possible to note the same signals at ~1000 nm, ~1200 nm and ~1500 nm [24].

Since the properties of the system under consideration will be explored in the NIR range of wavelengths, the calibration curve at λ=980 nm of the extinction coefficient with respect to the composition of the phantoms was extrapolated (Fig. 13). From this calibration and by comparing the results with literature, it was decided to choose a representative phantom composition to work with. A composition of 1% in Intralipid® was selected since its extinction coefficient in the NIR range is similar to the value reported for in vitro brain tissue [25]. The graph also reports the value of the extinction coefficient calculated each time a new tissue phantom was prepared and characterized.

An estimation of the time delay caused by the non-ballistic trajectory of photons through the tissue was calculated. Based on literature [25], representative values of reduced scattering coefficient and absorption coefficient of brain tissue in the NIR range were selected. The average path length ⟨L⟩ - i.e. the distance travelled by a photon within the tissue (discussed in paragraph 2.3.2) - was calculated by using the following expression [20]:

$$\langle L \rangle = \frac{\sqrt{3\mu_S'}}{2\sqrt{\mu_a}} \frac{l^2\sqrt{3\mu_S'\mu_a}}{l\sqrt{3\mu_S'\mu_a} + 1}$$

Where $l$ is the hypothesised thickness of the tissue, $\mu_s'$ is the reduced scattering coefficient and $\mu_a$ is the absorption coefficient. From this result, it is possible to calculate the induced time delay $\delta\tau$ in luminescence lifetime, which is [20]:

$$\delta\tau = (\langle L \rangle - l)\frac{n}{c}$$

where $n$ is the refractive index of tissue and $c$ is the speed of light in vacuum. Finally, it is also possible to calculate the tissue-induced temperature uncertainty $\delta T_{tissue}$ as following:

$$\delta T_{tissue} = \left(\frac{dT}{d\tau}\right)\delta\tau$$

The values used and the results obtained are summarized in Fig. 14. As expected, the time delay increased as the thickness of the tissue increased (from 0.1 to 1 cm), however its magnitude was very low, in the order of tenths of nanoseconds. As a consequence, the magnitude of the temperature uncertainty induced by the tissue was likewise very low ($10^{-4}$-$10^{-5}$ °C) and it could be neglected.

### 4.3.4. Temperature evolution of phantom's extinction spectrum

The evolution with temperature of the extinction spectrum of the phantom with composition corresponding to 1% of Intralipid® was then investigated. The phantom was synthesized directly in a cuvette with optical path length of 2 mm and the temperature controller (Q-pod) was placed inside the spectrophotometer in order to enable the selection of the desired temperature. The spectra were recorded based on the experimental conditions that are used for the emission measurements: the temperature was changed by 1 °C in the range between 30-45 °C, measuring in the wavelength interval from 900 nm to 1120 nm. The extinction coefficients were then calculated and reported in function of the wavelength (Fig. 15). The results of these measurements is that the extinction coefficient decreases in a comparable way by increasing the temperature.

## 4.4. NPs characterization: initial measurements

After the characterization of tissue phantoms, the NPs properties were investigated. In order to enable lifetime and emission measurements, a plastic microchannel was filled with 60 µl of the NPs water dispersion. This conformation allowed to place pieces of tissue phantoms on top of the luminescent NPs, avoiding sample waste.

### 4.4.1. Lifetime measurements

Lifetime measurements were performed by using an Optical Parametric Oscillator in order to confirm the dependence of NPs lifetime on temperature. The temperature of the NPs was controlled by means of a heating plate and changed with a step of 2 °C in the range between 32-46 °C. The decay curves collected (Fig. 16a) were analyzed, and the average lifetime was calculated as follows:

$$< \tau_{avg} > = \frac{\beta}{\tau} \Gamma\left(\frac{1}{\beta}\right)$$

the parameters β and τ were obtained by fitting the decay curves by means of a stretched exponential function:

$$I(t) = I_0 \cdot e^{-\left(\frac{t}{\tau}\right)\beta} + I_\infty \qquad 0 < \beta \leq 1$$

$I_0$ is the initial intensity at t=0, $\tau$ is the characteristic time constant, and β is the heterogeneity parameter [26].
Results obtained are reported in fig. 16b: the dependence of lifetime with temperature was confirmed, showing that $\tau_{avg}$ decreases as T is increased.

### 4.4.2. Emission measurements

NPs emission spectra were collected at the hypercube in the wavelength interval between 900-1120 nm, with spectral resolution = 5 nm, integration time = 5 s, with a laser power density of about 58 mW/cm$^2$. The temperature was changed in the range $T$ = 30-45 °C, with a step = 1 °C, in order to measure a calibration of the emission intensity vs. temperature. Emission measurements were also collected by placing phantoms of different thickness on the top of the channel with the NPs dispersion, as a first attempt to understand if they would induce spectral changes.

The unexpected result obtained was that, once the emission spectra of NPs were normalized by their maximum, their shape did not change with temperature (except for small fluctuations that could be considered negligible) (Fig. 17a). On the basis of these results, it was clear that the original project could no longer be realised, since the calibration of the emission as a function of temperature was no longer possible.

On the contrary, the interesting fact that came to light was that the shape of the emission spectra changed with the thickness of tissue phantoms (Fig. 17b). This finding proved to be an important turning point: actually, the fact that the shape of the emission spectra changes with the thickness of the tissue, could make it possible to trace the depth at which NPs are located inside a tissue. In addition, the shape is independent from the temperature, so it is possible to have a reliable readout of the depth only depending on the spectral distortion, regardless of the temperature at which the system is found.

# 5. New Project

On the basis of these results the system could be considered from another point of view: it can be seen as an orthogonal system, in which the two parameters (emission and lifetime) were independent. The lifetime changed only with temperature and it was not affected by the presence of the tissue, while the emission spectra was dependent on the features of the tissue phantom, such as composition or thickness, and it was not affected by the temperature. In particular, for this project it was selected to explore the influence of the phantom thickness on the shape of the emission spectra, mainly for two reasons related to possible future bio-applications:

1) the measure of the emission spectra could allow the prediction of the depth at which NPs are located inside the biological tissue;
2) the thickness-dependence of the shape of the emission spectra could also allow the use of such NPs as 3D capable thermometers.

## 5.1. Measurements of NPs emission spectra with phantoms

To verify this idea, hyperspectral images of the NPs were collected, after having placed the tissue phantom on top of the NPs. To have a continuous distribution of thicknesses, tissue phantoms were cut in a triangular shape (base = 2 cm, height = 1 cm), as shown in Fig. 18a. During the measurement, the whole sample was irradiated with the 808 nm laser and the images were collected with the following parameters in the temperature range between 30-45 °C with a step of 1°C: wavelength interval between 900-1120 nm, spectral resolution = 5 nm, integration time = 5 s, and laser power density of about 60 $mW/cm^2$ (Fig. 18b). One problem faced during these measures was the shrinking and the drying of the tissue phantom, due to the increasing temperature of the heating plate and to the prolonged exposure to the laser. Trying to reduce these effects, the piece of tissue phantom was changed every 2 °C, and it was also covered with a plastic slide.
For each measurement, a hyperspectral image like the one reported in Fig. 18c was obtained, in which it's clearly distinguishable that the intensity of the emitted light decreases with the thickness of the tissue phantom.
In a first analysis, to understand the entity of tissue-induced spectral changes, 5 regions of the images were selected, corresponding to 5 different thicknesses of the tissue, and

for each region the average emission spectrum was collected. The comparison between the normalized spectra confirmed considerable changes in the shape of the curve, with the same behaviour for each temperature (Fig. 19).

## 5.2. Dimensionality Reduction: Principal Components Analysis

At this point, since the results obtained were very promising, it was decided to apply dimensionality reduction (DR) techniques to better visualize the dependence of spectral changes with the thickness of the phantom.

### 5.2.1. Introduction to Dimensionality Reduction techniques

It's easy to understand that the calibration of this luminescent thermometer has generated a large dataset (intensity vs. several wavelengths vs. tissue thickness at different temperatures). Therefore, the use of dimensionality reduction algorithms and machine learning techniques was necessary to obtain a simplified representation of the dataset and to have a better comprehension of the information contained in those data. Dimensionality reduction can be defined as the transformation of data from a high-dimensional space into one with lower dimensionality such that the final representation retains most of its meaningful properties [18].
For instance, the employment of machine learning techniques could be a breakthrough for luminescence thermometry since it allows the complete use of the data contained in luminescence spectra. Luminescence thermometry is normally performed only on a single temperature-sensitive spectral feature of the emission spectra (e.g. intensity, luminescence intensity ratio (LIR), spectral shift, luminescence bandshape or bandwidth, etc.), but thermal information can be contained in the entire spectrum; the discarded information can lead to a misunderstanding of the real performance of the thermometer [27].

DR techniques act in two ways: by removing redundant input features and by transforming the input data to show information in a more representative form. In a linear DR method (Fig. 20), the process focuses on the linear transformation of the original variables, and an example of such technique is the so-called principal component analysis (PCA). Also non-linear DR approaches are possible, including for

example t-distributed stochastic neighbour embedding (t-SNE) or isometric mapping (Isomap) [18], but their use is beyond the scope of this study.

### 5.2.2. Principal Component Analysis

Principal component analysis (PCA) is a widely used technique in the analysis of large datasets, that aims to reduce the number of variables of a system, preserving as much information as possible. This method transforms an amount of *p* correlated variables into a smaller set of uncorrelated ones, since smaller datasets are easier to explore and visualize [18, 28, 29].

Considering to have all the data stored into a matrix with *n* columns (e.g. representing the number of measurements) and *m* rows (e.g. wavelengths at which the intensity is measured), the first step is the standardization of these data, so that each of them contributes equally to the analysis. The normalization method applied is the standard normal variate (SNV) method, in which every value is obtained by subtracting the mean value and dividing by the standard deviation [18, 28]:

$$z = \frac{value\ (n,m) - mean\ value}{standard\ deviation}$$

Note that PCA does not need to be based on values that have the same dimensionality, since the normalization allows to create another adimensional matrix that is used for the mathematical analysis.

Once that the dataset is normalized, the covariance matrix can be computed. Covariance is a statistical concept that quantifies the degree to which two random variables change together. It measures the relationship between these variables: a positive covariance indicates that they tend to increase or decrease simultaneously; a negative covariance indicates that the variables are inversely correlated, and one increases while the other decreases. Specifically, the covariance between two variables is calculated as the expected value of the product of their deviations from their respective means:

$$Cov(X,Y) = \frac{\Sigma(X_i - \bar{X})(Y_j - \bar{Y})}{n}$$

The covariance matrix, denoted as Σ, is a square matrix used in statistics and linear algebra to provide a comprehensive summary of the covariance relationships among multiple random variables within a dataset. Each element of this matrix represents the covariance between pairs of variables, with diagonal elements indicating the variances of individual variables and off-diagonal elements representing covariances. In essence, the covariance matrix encapsulates the degree and direction of linear relationships between

variables, helping analysts understand how they co-vary. If $p$ is the number of dimensions of the system, the covariance matrix is a $p \times p$ matrix, symmetric with respect to the main diagonal, formed by the covariances associated with all possible pairs of the initial variables [28].

At this point, in order to determine the new set of variables to use for the new description of the system, the eigenvectors and the eigenvalues of the covariance matrix must be computed. These new variables are the so-called Principal Components (PC), and they are uncorrelated linear combinations of the initial variables, organized in such a way that the variance is maximized [28, 29]. Geometrically speaking, it is possible to consider the points of a $p$-dimensional dataset to form a $p$-dimensional ellipsoid: PCs are the axes of such ellipsoid that capture most of the information of the dataset [18] (Fig. 21a). Since the number of PCs is equal to the number of variables in the dataset, they are organized in such a way that the first principal component (PC1) accounts for the largest possible variance in the data set [28].
Therefore, PCs are obtained from the eigenvectors of the covariance matrix, while the eigenvalues are simply coefficients that give the amount of variance carried by every principal component [28]. The eigenvectors are then sorted according to their eigenvalues in descending order. This organizes the PCs in order of significance: the higher the eigenvalue, the more information of the dataset the eigenvector explains (Fig. 21b). To compute the percentage of variance accounted for by each component, each eigenvalue is divided by the sum of all eigenvalues, and then the minimal number of eigenvectors that satisfies a previously established criteria (for instance, accounting for 90% of the variance of the original data) is found [18].
Finally, the original data must be projected onto the selected PCs in order to convert the representation of the system from the original basis to the new basis obtained from the PCA analysis.

*The algorithm applied in the project was written by Dr. Erving Ximendes.*

### 5.2.3. PCA in the project: results

The principal component analysis was applied for the analysis of the emission spectra, since their dependence with the thickness of the tissue could be better visualized in less

dimensions. However, before applying the algorithm for PCA, the data had to be pre-processed in order to create the initial matrix. Since PCA works with a very big amount of data, every hyperspectral image was divided in smaller regions of interest, as shown in fig. 22 (5 divisions in the x direction and 50 divisions in the y direction).

The average spectrum was extrapolated from each smaller rectangular region, it was normalized, and the values of intensity corresponding to wavelengths with no significant signal were removed. Hence, the wavelength range considered for this analysis was 935-1080 nm, where the emission peaks of Yb and Nd ions are present.
At this point the initial matrix for PCA could be created, considering the intensity at different thicknesses (ζ) and temperatures (*T*), for all the wavelengths (λ) in the selected interval:

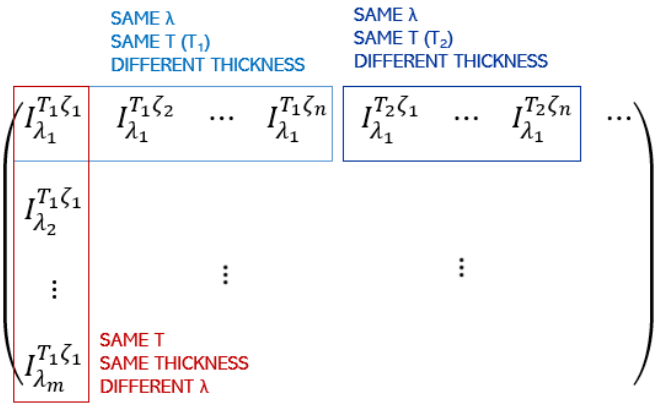


PCA was then applied starting from this matrix and the principal components for the new representation were found. What was revealed by this analysis is that, alone, the first principal component (PC1) explained nearly 94% of the dataset (Fig. 23), and for this reason, it was decided to use only PC1 and explore its dependence on the thickness of the tissue.

The tissue was made so that the thickness changed from around 0.1 cm to 1 cm, in a continuous manner (for this reason it was cutted in a triangular shape). By plotting the values of PC1 versus this range of thicknesses, the graph shown in fig. 24a was obtained: with this new representation it is easier to visualize the thickness-dependence of PC1 and consequently, of the emission spectra. In particular, the important resulting information was that PC1 varied in an unique and unambiguous manner in the range of thickness between 0.3-0.9 cm.

In addition, by knowing the temperature evolution of the extinction coefficient of the tissue, a principal component regression can be done to predict the thickness of the tissue for every temperature. The results of this simulation have demonstrated that for every temperature the behaviour of PC1 is more or less equal (Fig. 24b): it changes with thickness in the same way, proving that it is possible to predict the depth of NPs even working at different temperatures.

## 5.3. Basis for 3D Luminescence thermometry

In addition to an easier description of the system, one important result obtained by PCA is that, by using PC1 as the new basis for the representation, it is also possible to predict the thickness of the tissue. Taking advantage of this achievement, it was explored the possibility to reconstruct the 3D image of a simple geometry (i.e. a cone).

### 5.3.1. Emission measurements

As a first step, emission spectra of the same NPs were collected again, this time changing a little the set up of the system. First of all, a capillary was filled with the water dispersion of NPs, in order to allow their insertion inside the tissue (they were not injected with a syringe to avoid the loss of the NPs at every measure). By using a 3D-printed mold, conic shaped tissue phantoms were prepared (Fig. 25a); the composition was equal to the tissue phantoms used in the previous analysis, with the same relative amount of Intralipid® emulsion (1% of the total volume). Then, the capillary containing the dispersion of NPs was inserted in the middle of the phantom, perpendicular to the base of the cone; again the tissue was covered by a transparent plastic foil, properly-shaped, in order to limitate the drying and the shrinking of the tissue, even if in this case, these processes were less significant since the measurements were collect at room temperature. This sample was then placed on a special support surrounded by a rotating platform on which 4 NIR mirrors (ThorLabs, PFSQ10-03-M01, protected gold coated mirrors) were mounted perpendicularly to one another (Fig. 25b). The movement of the platform was managed by a goniometer which allowed the control of the rotation up to tenths of degree. The whole system was placed in the hypercube for collection of the emission measurements.

The rest of the set-up was maintained the very same, with the laser above, in order to irradiate the nanoparticles from the top. Hyperspectral images were then acquired at room temperature, with the following conditions: interval of wavelength between 930-1080 nm, spatial resolution = 5 nm, integration time = 5 seconds, laser power density around 80 mW/cm$^2$.
A hyperspectral image was collected for every 5° step in the clockwise direction of the rotating platform, until the 90° position was reached, so that the whole space was covered (Fig. 26). The spot in the middle of the image corresponds to the signal coming directly from the NPs in the capillary, that was placed right under the laser (parallel to the beam), while the 4 signals around, perpendicular one to each other, are the signals coming from the reflections on the mirrors. In these reflected signals, it is clearly visible that the intensity of the detected light decreases moving down along the height of the cone, as the thickness of the tissue increases.

### 5.3.2. DR for image reconstruction

When all the hyperspectral images were collected, the emission spectra was extrapolated from each point of the image where a signal was detected, considering all the different heights of the NPs inside the phantom and all the different angles of measurement (Fig. 27). The spectral data were then analyzed as before, applying the Principal Component Analysis. Based on PC1, the same regression was applied to obtain an estimation of the thickness of the tissue: for each combination of angle and height, a predicted thickness was obtained. Such predicted value could be compared with the real thickness of the tissue phantom and could be used for the 3D image reconstruction. Indeed, this could be done by plotting in three dimensions PC1 in function of the predicted thickness (which gives a plot similar to the one represented in fig. 23a), by considering all the angles of measurement.

The 3D image reconstructed and the real shape of the tissue are shown in fig. 28a. At first sight they seem quite different, but overlapping them it appears immediately clear that the reconstruction is accurate enough in the range of thicknesses between 0.3-0.9 cm (Fig. 28b), that is the one in which the relation of PC1 with the thickness is unambiguous (Pharagraph 5.2.3.). This reconstructed shape is not perfect because not all the points

follow the linear trend necessary to have the cone, but the reason for this can be attributed to low level of signal of the emission measurements, which probably distorts the spectra even more than expected.

# 6. Conclusions and future perspectives

The principal aim of this project was to build up the case for the realization of 3D capable nanothermometers, by means of dimensionality reduction techniques (PCA). Actually, this analysis enabled a reliable prediction of the thickness of the tissue phantom, making it possible to estimate the depth at which NPs are located when they are injected into a biological system. In addition, a rough reconstruction of the 3D shape of a conic tissue was achieved, giving the first positive results in the realization of such systems, even though there is still much room for improvement.

The first factor to consider could be the influence of different spatial profiles of the excitation source, exploring if they could extend the range in which the inference of the thickness is made (point source vs. line source, etc.), as well as how the direction of the incoming light will affect the measures. In this work, in fact, the laser was always placed in such a way to illuminate the sample from the top, but in this case two phenomena occur: the attenuation of the emitted light, and the attenuation of the incoming light. Hence, considering to have NPs at two different depths inside a tissue, not only the emitted light is attenuated in different ways (since light has to travel different distances to exits from the tissue), but also the excitation of the NPs placed at the major depth is reduced with respect to the excitation of more superficial NPs.

For this reason, one strategy for improving the system could be doing different calibrations changing the position of the laser, which can be useful to understand all the phenomena happening (e.g. placing it below the tissue, even if it is not what happens for real systems).

Upon addressing the above issues, the system may be applied in vivo, for instance, to estimate the volume or the shape of a tumor inside a biological tissue, by simultaneously measuring temperature changes.

# 7. References


[1] IUPAC, Compendium of Chemical Terminology, 2nd ed. (the "Gold Book"), compiled by A. D. McNaught and A. Wilkinson, Blackwell Scientific Publications, Oxford (1997). Online version (2019-) created by S. J. Chalk. https://doi.org/10.1351/goldbook

[2] J. J. Carvajal, M. C. Pujol, (2023) "Introduction to Luminescence Thermometry", in "Luminescent Thermometry", J. J. Carvajal, M. C. Pujol (eds.), *Springer Science and Business Media LLC*. https://doi.org/10.1007/978-3-031-28516-5

[3] P. Atkins, J. de Paula, (2002), "Atkins' Physical Chemistry" (7th ed.), Oxford University Press.

[4] G. Pettinari, A. Polimeni, M. Capizzi, (2012), "Photoluminescence: A Tool for Investigating Optical, Electronic, and Structural Properties of Semiconductors", in "Semiconductor Research: Experimental Techniques", A. Patane, N. Balkan (eds.), *Springer Series in Materials Science*, 150. https://doi.org/10.1007/978-3-642-23351-7

[5] M. R. Soboleski, J. Oaks, W.P. Halford, (2005), "Green fluorescent protein is a quantitative reporter of gene expression in individual eukaryotic cells", *The FASEB Journal,* 19(3), 1–20. https://doi.org/10.1096/fj.04-3180fje

[6] S. Wang, N. Li, W. Pan, B. Tang, (2012), "Advances in functional fluorescent and luminescent probes for imaging intracellular small-molecule reactive species", *Trends in Analytical Chemistry*, 39, 3–37. https://doi.org/10.1016/j.trac.2012.07.010

[7] J. C. G. Bünzli, S. V. Eliseeva, (2011), "Basics of Lanthanide Photophysics", in "Lanthanide Luminescence: Photophysical, Analytical and Biological Aspects", P. Hanninen, H. Harma (eds.), *Springer Series on Fluorescence*, 7. https://doi.org/10.1007/978-3-642-21023-5

[8] J. C. G. Bünzli, C. Piguet, (2005), "Taking advantage of luminescent lanthanide ions", *Chemical Society Reviews*, 34(12), 1048-1077. https://doi.org/10.1039/b406082m

[9] R. Marin, D. Jaque, (2021), "Doping Lanthanide Ions in Colloidal Semiconductor Nanocrystals for Brighter Photoluminescence", *Chemical Reviews*, *121*(3), 1425–1462. https://doi.org/10.1021/acs.chemrev.0c00692

[10] S. V. Eliseeva, J. C. G. Bünzli, (2010), "Lanthanide luminescence for functional materials and bio-sciences", *Chemical Society Review*, *39*(1), 189–227. https://doi.org/10.1039/B905604C

[11] M. Safdar, A. Ghazy, M. Lastusaari, M. Karppinen, (2020), "Lanthanide-based inorganic–organic hybrid materials for photon-upconversion", *Journal of Materials Chemistry C*, *8*(21), 6946–6965. https://doi.org/10.1039/D0TC01216E

[12] G. Sun, Y. Xie, L. Sun, H. Zhang, (2021), "Lanthanide upconversion and downshifting luminescence for biomolecules detection", *Nanoscale Horizons*, *6*(10), 766–780. https://doi.org/10.1039/D1NH00299F

[13] B. Zhang, X. Guo, Z. Zhang, Z. Fu, H. Zheng, (2022), "Luminescence thermometry with rare earth doped nanoparticles: Status and challenges", *Journal of Luminescence*, *250*, 119110. https://doi.org/10.1016/j.jlumin.2022.119110

[14] C. D. S. Brites, A. Millán, L. D. Carlos, (2016), "Lanthanides in Luminescent Thermometry", in "Handbook on the Physics and Chemistry of Rare Earths", *Elsevier*, 49, 339–427. https://doi.org/10.1016/bs.hpcre.2016.03.005

[15] K. L. Wong, J. C. G. Bünzli, P. A. Tanner, (2020), "Quantum yield and brightness", *Journal of Luminescence*, *224*, 117256. https://doi.org/10.1016/j.jlumin.2020.117256

[16] Y. Shen, J. Lifante, N. Fernández, D. Jaque, E. Ximendes, (2020), "*In Vivo* Spectral Distortions of Infrared Luminescent Nanothermometers Compromise Their Reliability", *ACS Nano*, *14*(4), 4122–4133. https://doi.org/10.1021/acsnano.9b08824

[17] A. Bednarkiewicz, L. Marciniak, L. D. Carlos, D. Jaque, (2020), "Standardizing luminescence nanothermometry for biomedical applications", *Nanoscale*, *12*(27), 14405–14421. https://doi.org/10.1039/D0NR03568H

[18] E. Ximendes, R. Marin, L. D. Carlos, D. Jaque, (2022), "Less is more: Dimensionality reduction as a general strategy for more precise luminescence thermometry", *Light: Science & Applications*, *11*(1), 237. https://doi.org/10.1038/s41377-022-00932-3

[19] G. Keiser, (2016), "Light-tissue interactions", in "Biophotonics: Concepts to Applications", *Graduate Texts in Physics, Springer Singapore*. https://doi.org/10.1007/978-981-10-0945-7

[20] Y. Shen, J. Lifante, I. Zabala-Gutierrez, M. de la Fuente-Fernández, M. Granado, N. Fernández, J. Rubio-Retama, D. Jaque, R. Marin, E. Ximendes, A. Benayas, (2022), "Reliable and Remote Monitoring of Absolute Temperature during Liver Inflammation via Luminescence-Lifetime-Based Nanothermometry", *Advanced Materials*, *34*(7), 2107764. https://doi.org/10.1002/adma.202107764

[21] M. Tan, F. Li, N. Cao, H. Li, X. Wang, C. Zhang, D. Jaque, G. Chen, (2020), "Accurate In Vivo Nanothermometry through NIR-II Lanthanide Luminescence Lifetime", *Small*, 16, 2004118. https://doi.org/10.1002/smll.202004118

[22] B. W. Pogue, M. S. Patterson, (2006), "Review of tissue simulating phantoms for optical spectroscopy, imaging and dosimetry", *Journal of Biomedical Optics,* 11(4), 041102. DOI: 10.1117/1.2335429

[23] W. M. Piotrowski, R. Marin, M. Szymczak, E. Martín Rodríguez, D. H. Ortgies, P. Rodríguez-Sevilla, M. D. Dramićanin, D. Jaque, L. Marciniak, (2023), "Mn5+ Lifetime-Based Thermal Imaging in the Optical Transparency Windows Through Skin-Mimicking Tissue Phantom", *Advanced Optical Materials,* 11, 2202366. https://doi.org/10.1002/adom.202202366

[24] T. Muñoz-Ortiz, L. Abiven, R. Marin, J. Hu, D. H. Ortgies, A. Benayas, F. Gazeau, V. Castaing, B. Viana, C. Chanéac, D. Jaque, F. E. Maturi, L. D. Carlos, E. Martín Rodríguez, J. García Solé, (2022), "Temperature Dependence of Water Absorption in the Biological Windows and Its Impact on the Performance of $Ag_2S$ Luminescent Nanothermometers", *Particle & Particle Systems Characterization*, 39(11), 2200100. https://doi.org/10.1002/ppsc.202200100

[25] Madsen, S. J. (Ed.), (2013), "Optical Methods and Instrumentation in Brain Imaging and Therapy", Springer New York. https://doi.org/10.1007/978-1-4614-4978-2

[26] D. H. Ortgies, M. Tan, E. Ximendes, B. del Rosal, J. Hu, L. Xu, X. Wang, E. Martín Rodríguez, C. Jacinto, N. Fernandez, G. Chen, D. Jaque, (2018), "Lifetime-Encoded Infrared-Emitting Nanoparticles for in Vivo Multiplexed Imaging", *ACS Nano*, 12(5), 4362–4368. https://doi.org/10.1021/acsnano.7b09189

[27] J. Cui, W. Xu, M. Yao, L. Zheng, C. Hu, Z. Zhang, Z. Sun, (2023), “Convolutional neural networks open up horizons for luminescence thermometry”, *Journal of Luminescence*, 256, 119637. https://doi.org/10.1016/j.jlumin.2022.119637

[28]https://builtin.com/data-science/step-step-explanation-principal-component-analysis

[29] I. T. Jolliffe, J. Cadima, (2016), “Principal component analysis: A review and recent developments”, *Philosophical Transactions of the Royal Society A: Mathematical, Physical and Engineering Sciences*, 374(2065), 20150202. https://doi.org/10.1098/rsta.2015.0202

# Appendix 1: Temperature measurements

Every time the heating plate was involved in a measure, the temperature evolution was also followed by means of a thermocouple, to understand the level of discrepancy between the set values and the real values. The same was done for the measurements involving the Q-pod. The thermocouple data were recorded by PicoLog thermocouple data logger. In this section, graphs and data reporting the temperature evolution are shown for each calibration measure.

*Temperature evolution within the Q-pod during extinction measurements*

Extinction measures were collected by means of the Q-pod to have the possibility to select the sample temperature. To verify the correspondence between set values and real values, the temperature inside the Q-pod was measured by means of a thermocouple. The real temperature was computed by averaging about 200 values selected in an area of the curve in which the temperature was stable (e.g. highlighted region in fig. 1A). Results (set T, real $T_{avg}$, and standard deviation $\sigma$) are reported in the table below, while the set-up was shown in fig. 2A.

*Temperature evolution of the heating plate during lifetime measurements*

Instead, the use of the heating plate was required to change the temperature of the sample during lifetime measurements. Temperature evolution was followed by means of a thermocouple specific for surfaces, and the data are reported in the graph and tab. Below (Fig. 3A). The regions highlighted in yellow are the ones used to compute real temperatures, always by averaging about 200-250 values. The regions within the red rectangles are signals arising from temporary malfunctioning of the heating plate, but they have not affected the measures.

*Temperature evolution of the heating plate during emission measurements*

The heating plate was also used to change the temperature of the sample during emission measurements at the hypercube. Again, real temperatures were computed (together with the standard deviation) by averaging 200-250 values of the yellow regions in the graph below (Fig. 4A). Signals in blue regions were considered as artifacts, since they appeared as soon as the laser was turned on and they immediately disappeared when it was switched off. Even considering the fact that the laser could induce some heating, its power was not enough to ensure such an instantaneous increase in the temperature of the NPs. The remaining signals indicated by arrows are due to the moments in which the phantom tissue was changed, so they must not be considered.

# Appendix 2: experimental set-up

*Tissue phantoms*

*Extinction measurements set-up*

*Lifetime measurements set-up*

*Emission measurements set-up*

# Acknowledgments

At the end of this work, I would like to express my deepest gratitude to all the people who played significant roles, not only for this project, but also during my studies.

First, I would like to thank my supervisor, prof. Patrizia Canton, for her help and advice with this thesis, and for the big opportunity she gave me proposing to conduct the project at NanoBIG group.

A special thanks to dr. Erving Ximendes for his assistance at every stage of the research project, and to dr. Riccardo Marin for his availability and support, without whom my internship would not be possible. I would like to extend my thanks also to all the researchers of the NanoBIG group in Madrid, for their warm hospitality and their helpfulness.

I am also grateful to Emily, Anna, Alex and all my other classmates for having shared with me two fantastic years.

Lastly, I would like to mention my family - my dad, my mum, my sisters Valentina and Elena, and Simone - for their support and belief in me during this journey.